Quantifying Topographic Influence on Irradiance Transfer in Permanently Shadowed Regions

Prasun Mahanti[1], Mark Robinson[1]

[1]School of Earth and Space Exploration, Arizona State University, Tempe, Arizona, USA - (pmahanti.lroc@gmail.com)

Keywords: Permanently Shadowed Region, View factors, Topographic Influence, Secondary illumination, ShadowCam

Abstract

In permanently shadowed regions (PSRs), the surface temperature is influenced by secondary illumination, which changes daily and seasonally due to the sunlight reflected by the surrounding terrain. Understanding how topography affects the transfer of radiant energy can help us quickly interpret the thermal behavior using available topographic data. The amount of radiant energy transferred from a sunlit lunar surface to a PSR depends on the distance and orientation of the sunlit surface to the PSR, and is represented by view factors. In this study, we introduce an approach to systematically represent the combined effects of multiple surfaces using statistical analysis applied to view factor maps. We demonstrate that our proposed approach can explain the contrasting temperatures of two PSRs at the lunar south pole. We verify our theoretical findings using PSR images acquired by the ShadowCam instrument aboard the Danuri lunar orbiter

1. Introduction

Thermal balance within Permanently Shadowed Regions (PSR) depends on local topography (Hodges Jr, 1980, Vasavada et al., 1999, Ingersoll et al., 1992), which controls the scattered irradiance (visible and thermal). Temperatures inside PSRs result from the thermal balance between secondary illumination (visible wavelength), re-radiated thermal energy, and heat from the interior of the Moon. The scattered radiation is the dominant component in the overall thermal balance at the PSRs (Buhl et al., 1968, Lucey et al., 2021) - heat flow from the lunar interior contributes minimally (Paige et al., 1992). PSRs are heated to the extent the PSR can ’see’ sunlit surfaces (e.g., crater walls). The possibility of volatile cold-trap temperatures (e.g., summer maximum temperature $< 110K$ for water) is reduced by topography that scatters more of the direct sunlight (primary illumination) into the PSR (as secondary illumination), adding to the thermal input. Low maximum summer temperatures imply dim secondary illumination, and images of such PSRs have a low signal-to-noise ratio (Lucey et al., 2021). The quantification of topographic influence is complicated since the effect is cumulative (from multiple topographic facets) and time-variable (depending on the subsolar point). Earlier efforts investigating topographic influence (Buhl et al., 1968, Ingersoll et al., 1992, Paige et al., 1992, Carruba and Coradini, 1999, Vasavada et al., 1999, Siegler et al., 2011) relied on idealized crater shapes to derive simple theoretical representations and closed-form thermal solutions. Here, we quantify topographic influence based on view factor maps, which encode the geometry between interacting topographic facets (Cohen et al., 1993). Using topographic influence maps (TIM) and the knowledge of direct illumination, we show why secondary illumination will be much higher for PSR B (Spudis crater, 89.506°S, 280.685°E, 53.3 km^2) than PSR A (88.997°S, 19.199°E, 55.4 km^2). We also characterize the time-varying topographic influence to understand why PSR A is better suited for being a cold trap (summer maximum T $<$ 70K) than PSR B (summer maximum T $>$ 110K). Additionally, we verify the contrasting levels of secondary illumination at the two PSRs using images from ShadowCam (Robinson et al., 2023), a PSR imaging camera onboard the KPLO (Danuri) (Kim, 2022) spacecraft.

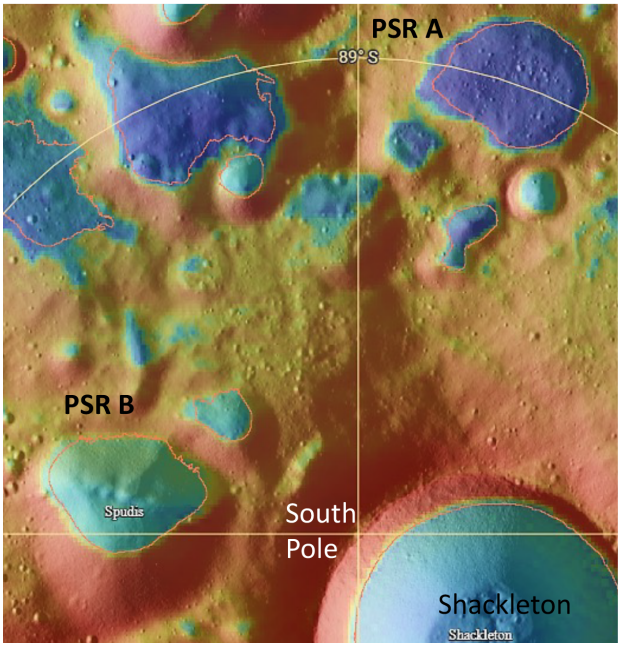

Figure 1. Location of PSR A and B. PSR B (in Spudis crater) is closer to the south pole but has higher summer maximum temperatures than PSR A

2. Secondary illumination at PSRs

To accurately calculate secondary illumination, it is essential first to outline the map area, including the PSR and nearby topography, which can contribute to the reflected light. This is done on a case-by-case basis by analyzing the topography around the PSR and considering the amount of direct solar illumination, line-of-sight from directly illuminated topography and PSR, and the distance of directly illuminated topography from the PSR. For the selected PSRs, a square map area with 30 km sides centered on the PSR was deemed sufficient for robust computation of the secondary illumination. Once the map area is defined, a shapefile for the PSR and topography cropped to the map area is used to obtain viewsheds and view factor maps.

Viewsheds are binary maps indicating the presence (or absence) of line-of-sight from PSR locations to the rest of the map area. View factor maps contain numerical coefficients (view factors or form factors) representing the fraction of primary illumination reflected from a source outside the PSR to a receiver inside the PSR (Cohen et al., 1993). The view factor ϕ_{ij} is expressed as

$$\phi_{ij} = \frac{A_j \cos\theta_1 \cos\theta_2}{\pi d^2} \quad (1)$$

following the geometry shown in Fig.2. In addition, the view factor ϕ_{ij} is defined to be zero if there is no direct line of sight between facets j and i. A_j is the area of the directly illuminated facet, and d is the distance of the line-of-sight connecting the two facets. The emission angle of the outgoing scattered ray at the directly illuminated facet is θ_1 and the incidence angle of the incoming scattered ray at the secondary illuminated facet is θ_2, and n_1 and n_2 are the facet normals. For the chosen subsolar point, θ_1 depends only on the directly illuminated facet j, while θ_2 depends on both i and j.

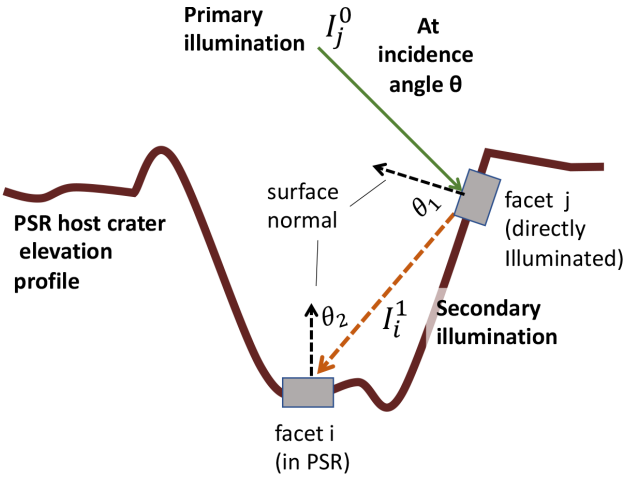

Figure 2. Concept of secondary illumination in lunar PSRs. Primary illumination (green) and secondary illumination (orange) show the interaction between one directly illuminated topographic facet(j) and one topographic facet(i) in PSR.

Local topography strongly affects the view factor. Surface normals need to be collinear and opposite for maximum magnitude, and $\phi_{i,j}$ inversely varies with d^2. Thus, planes facing each other and close together have larger view factors. Low amounts of secondary light are expected in the flat areas of lunar craters due to near-parallel facet orientations and increased incident secondary light where the slopes of the crater's inner wall are steep. In the example (Fig. 3) for PSR B, we see that locations in close proximity may not have a large view factor magnitude unless there is a slope. Also, note that the areas outside the PSR boundary are the main contributing sources. Within the PSR, the view factor magnitudes are more useful when computing tertiary (two reflections) or higher-order illumination.

The secondary illumination irradiance I_i received at a PSR location i is approximated (single bounce) as

$$I_i \cong \sum_{j=1}^{N_1} \alpha_j \phi_{ij} I_j^0 \quad (2)$$

Details of the modeling methods can be found in (Mahanti et al., 2021). Alternately, for clarity with time variable raster data,

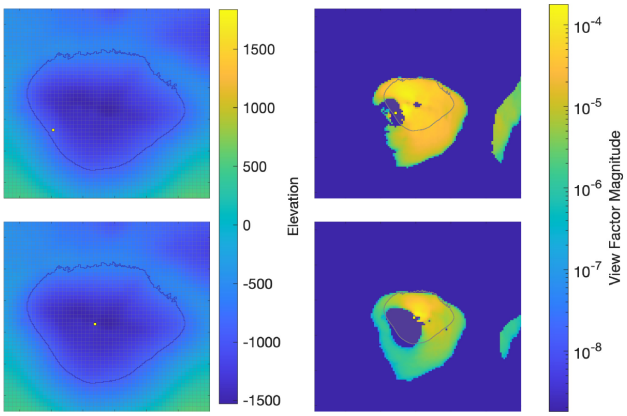

Figure 3. View factor maps for observers at two different locations within PSR B. Brighter colors indicate larger view factor magnitude.

we re-write the same expression as

$$S(x,y,t) \cong \sum_{j=1}^{N_1} \alpha_j \phi_{ij} P^0(x,y,t) \quad (3)$$

for a DTM raster $Z(x,y)$, where Z is the elevation, and at time t the secondary illumination is $S(x,y,t)$, and the primary illumination is $P^0(x,y,t)$

The primary illumination map and the view factor maps are used to compute the secondary illumination for the topographic facets within the boundary of PSRs. For simplicity, we assumed a Lambertian photometric function and uniform albedo (for primary illumination scattering).

3. Characterizing topographic influence

To understand the effect of topography in terms of view factors, we discuss a simple example of secondary illumination (Figure 4) with two 'observers' (1 and 2; pixels in the PSR) and two sources (A and B; directly illuminated pixels in sunlit zones) The time (t) variable secondary illumination reaching pixels 1 and 2 are $S_1\,(t)$ and $S_2\,(t)$ and the primary illumination reaching pixels A and B are $P_A^0\,(t)$ and $P_B^0\,(t)$. The expressions for secondary illumination is then given by

$$S_1\,(t) = \alpha_A \phi_{1A} P_A^0\,(t) + \alpha_B \phi_{1B} P_B^0\,(t) \quad (4)$$

and

$$S_2\,(t) = \alpha_A \phi_{2A} P_A^0\,(t) + \alpha_B \phi_{2B} P_B^0\,(t) \quad (5)$$

A compact representation of the above equations is

$$\begin{bmatrix} S_1\,(t) \\ S_2\,(t) \end{bmatrix} = \begin{bmatrix} \alpha_A\phi_{1A} & \alpha_B\phi_{1B} \\ \alpha_A\phi_{2A} & \alpha_B\phi_{2B} \end{bmatrix} \begin{bmatrix} P_A^0\,(t) \\ P_B^0\,(t) \end{bmatrix} \quad (6)$$

Statistics for time-aggregated secondary illumination are computed from the secondary illumination of individual pixels. In the case of the time-averaged secondary illumination (i.e. average statistics obtained over a temporal cycle) the average of the sum

$$S(t) = S_1\,(t) + S_2\,(t) \quad (7)$$

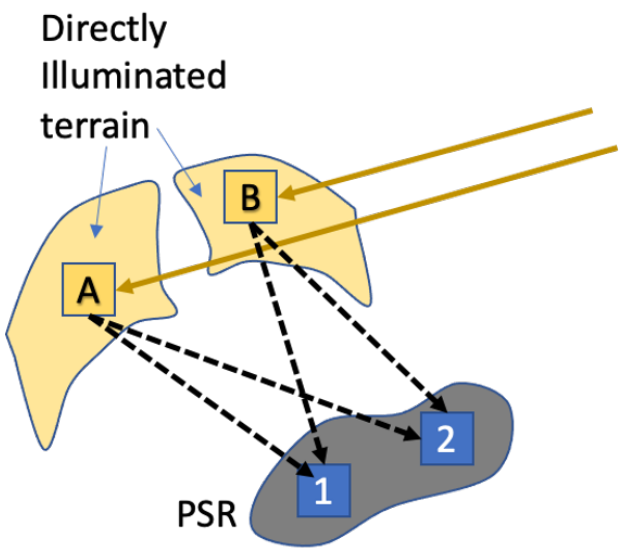

Figure 4. General schematic illustrating secondary illumination between two pairs of source (A and B - directly illuminated) and observer (1 and 2 - within PSR) topographic facets.

is given by the sum of the averages

$$\langle S(t)\rangle = \langle S_1(t) + S_2(t)\rangle \tag{8}$$

Using the expressions from (4) and (5) we get

$$S(t) = \alpha_A P_A^0(t)(\phi_{1A} + \phi_{2A}) + \alpha_B P_B^0(t)(\phi_{1B} + \phi_{2B}) \tag{9}$$

which can be written compactly as

$$S(t) = \begin{bmatrix} \alpha_A P_A^0(t) & \alpha_B P_B^0(t) \end{bmatrix} \begin{bmatrix} \phi_{1A} + \phi_{2A} \\ \phi_{1B} + \phi_{2B} \end{bmatrix} \tag{10}$$

The time-averaged secondary illumination $\langle S(t)\rangle$ is

$$\langle S(t)\rangle = \begin{bmatrix} \alpha_A \left\langle P_A^0(t)\right\rangle & \alpha_B \left\langle P_B^0(t)\right\rangle \end{bmatrix} \begin{bmatrix} \phi_{1A} + \phi_{2A} \\ \phi_{1B} + \phi_{2B} \end{bmatrix} \tag{11}$$

where

$$\left\langle P_A^0(t)\right\rangle = \frac{1}{T}\int_0^T P_A^0(t)$$

is the continuous time average of the primary illumination over the period T. For simulations, however, we obtain discrete-time samples of the time axis. In our simulations of secondary illumination, the illumination magnitude is dependent on subsolar latitude (λ_1) and subsolar longitude (λ_2), which are both dependent on time.

$$(\lambda_1, \lambda_2) \propto f(t) \tag{12}$$

Using $[\lambda_1]$ and $[\lambda_2]$ to represent the discrete subsolar latitude and longitude axis and $[\tau]$ to represent the discrete time axis we have the following expression for the discrete-time average over the subsolar longitude (and represents diurnal average) for the primary illumination at pixel A

$$\widehat{P_A^0[\lambda_2]} \propto \sum_{\lambda_2=0}^{\lambda_2=359} P_A^0(\lambda_2) \tag{13}$$

A similar expression can be obtained for pixel B. The average secondary illumination can then be written as

$$\widehat{S[\tau]} = c\begin{bmatrix} \widehat{P_A^0[\lambda_2]}[\lambda_1] & \widehat{P_B^0[\lambda_2]}[\lambda_1] \end{bmatrix} \begin{bmatrix} \phi_{1A} + \phi_{2A} \\ \phi_{1B} + \phi_{2B} \end{bmatrix} \tag{14}$$

where c is the constant that represents any normalization and effects of albedo. The diurnal average still varies with the subsolar latitude $[\lambda_1]$, i..e seasonal dependence and represents the time variation. We rewrite the above equation as

$$\widehat{S[\tau]} = cP_{av}^0[\lambda_1]\,\Psi \tag{15}$$

where

$$P_{av}^0[\lambda_1] = \begin{bmatrix} \widehat{P_A^0[\lambda_2]}[\lambda_1] & \widehat{P_B^0[\lambda_2]}[\lambda_1] \end{bmatrix} \tag{16}$$

and

$$\Psi = \begin{bmatrix} \phi_{1A} + \phi_{2A} \\ \phi_{1B} + \phi_{2B} \end{bmatrix} = TIM \tag{17}$$

We can rewrite $P_{av}^0[\lambda_1]$ as $P_{av}^0[x, y, \tau]$ to represent the diurnally averaged primary illumination at the point (x, y). Note that the $P_{av}^0[\lambda_1]$ is time-varying, and the τ variable represents samples from the subsolar time. $\Psi[x, y]$ represents the topographic influence map (TIM) and is spatially varying. At each position (x,y) of a directly illuminated source pixel, the TIM is the sum of all the view factors from the source position to observer positions in the PSR. Following the convention adopted in [2], we get

$$\Psi_i = \sum_j \phi_{ij} \tag{18}$$

Note that Ψ_i does not include any albedo term and is purely dependent on topography.

4. Methods

Contribution to secondary illumination is analyzed using raster representations of the direct illumination ($P_{av}^0[x, y, \tau]$; accumulated over time) and topographic influence ($\Psi[x, y]$) from the cumulative effect of all view factors. Using both $P_{av}^0[x, y, \tau]$ and $\Psi[x, y]$ we get the irradiance transfer function.

4.1 Normalized primary illumination maps

The normalized primary illumination map is obtained from direct illumination maps of the PSR region for subsolar latitude increments of 0.1° and longitude increments of 10°. The incident solar vector is a function of the subsolar latitude (affects the elevation of the solar vector, varies between $\pm 1.586^\circ$ for the Moon) and the subsolar longitude (azimuthal direction of the solar vector, varies between 0° to 359°). Direct illumination map cell values are proportional to $\cos(\theta_i)$ where θ_i is the incidence angle. The primary illumination is computed over the map area but uses a topography extending to 80S. The maximum value is obtained at each cell (x,y) from all the direct illumination maps (across subsolar latitude -1.586°to 0°here).

Similarly, the average value can be obtained at each cell (x,y) by aggregating $P^0_{av}[x, y, \tau]$ across the subsolar latitude (or τ with respect to subsolar time). Finally, for comparison, each map is normalized by the maximum value of direct illumination (from all cells across both maps).

4.2 Topographic influence maps (TIM)

View factors represent the fractional irradiance transferred from a directly illuminated source topographic facet to a receiver topographic facet within the PSR. A larger view factor magnitude implies a larger transfer between the interacting facets. For a specific receiver location within the PSR, a single view factor map represents the fractional irradiance for all source locations. When all the view factor maps are combined (stack of viewfactor maps summed at each pixel x,y) the resulting map $\Psi[x, y]$ shows the magnitude of topographic influence for each source outside the PSR. Topographic influence maps illustrate the relative spatial contribution under uniform primary illumination outside the PSR boundary. For comparison across PSRs, the topographic influence can be normalized (e.g. to the maximum value); a value of one (Fig. 5A,B, bright yellow) indicates the location of the largest possible contribution for these two PSRs.

4.3 Irradiance Transfer function (ITF)

We define ITF as the time variable (varies with subsolar latitude; integrated over subsolar longitude) ratio of total irradiance transferred to the PSR (as secondary illumination) to the total irradiance received outside the PSR, e.g., if 100 $Wm^{-2}\mu m^{-1}$ is received as primary illumination that can potentially be transferred and 1 $Wm^{-2}\mu m^{-1}$ is actually transferred as secondary illumination, then the ITF value is 0.01. From our definitions of the diurnally averaged direct illumination map and TIM, the ITF at a pixel (x,y) can be written as

$$ITF(\tau) = \frac{\sum_i \Psi_i P^0_i[\tau]}{\sum_i P^0_i[\tau]} \tag{19}$$

In our computations we use the subsolar latitude $[\lambda_1]$ for time $[\tau]$.

Steps in our computation of ITF : The following steps lead to the computation of ITF from topography

- *Define the map area for the PSR and obtain the corresponding DEM and PSR shapefile*
- *Compute viewshed and view factor maps for all PSR pixels from the DEM and the PSR shapefile*
- *Compute topographic influence map $\Psi[x, y]$ from the viewfactors*
- *Compute the primary illumination irradiance map $P_o(x, y, t)$ from the DEM for subsolar time intervals*
- *Compute the diurnally averaged primary illumination irradiance map $P_o(x, y, \tau)$ from the DEM for subsolar latitude intervals*
- *Compute ITF(τ) from $P_o(x, y, \tau)$ and $\Psi[x, y]$ for each subsolar latitude interval*

4.4 ShadowCam PSR mosaics

ShadowCam images acquired over each of the two PSRs are merged to obtain a maximum radiance value map for each PSR (60 m/px) at each month. The maps include observations from January 2023 through July 2023, and at each month, the maps represent an aggregate up to that month.

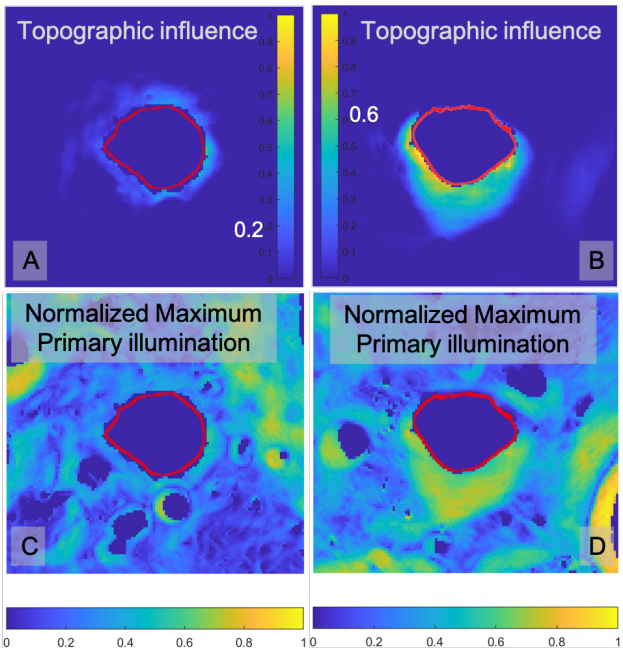

Figure 5. Top row (A and B) shows the topographic influence maps for PSR A and PSR B respectively. A normalized scale shows that the topographic influence of PSR B is larger. Bottom row (C and D) show the corresponding maximum normalized primary illumination maps where the maximum value at each pixel is obtained over the full subsolar time range of the computation of primary illumination

5. Results and Discussion

Topographic influence for PSR A (Fig. 5A) is symmetric from sunlit areas to ∼3 km from the PSR boundary, with some higher contributions from the right and lower contributions from the left, close to the PSR boundary. PSR B rests within a topographic amphitheater - the influence of topography is strongly asymmetric (Fig. 5B) in the top-to-bottom direction with significant contributions as far as ∼8 km towards the bottom, tapering down upwards on both left and right to near zero at the topmost PSR boundary. Further up, sunlit topography is too far from PSR B to contribute to the secondary illumination. Under identical and uniform primary illumination, PSR A would receive less secondary illumination than PSR B.

The normalized maximum primary illumination maps show whether illumination is available (how much at what distance) to transfer as secondary illumination (Fig. 5C,5D). PSR B has a higher magnitude of primary illumination available than PSR A (average maps also show a similar contrast between the two PSRs)

From the two maps, we can conclude that PSR A will not receive higher levels of secondary illumination since both factors, topographic influence and primary illumination, are low. Thus,

PSR A has a better chance of being a cold trap. For PSR B, both factors are high, and consequently, PSR B will always have higher secondary illumination and lower chances of being a cold trap.

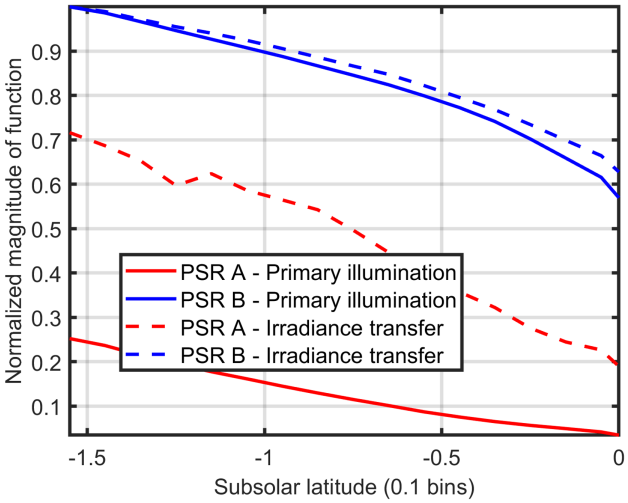

Figure 6. Irradiance transfer function and Average primary illumination vs subsolar latitude

TIM and the normalized maximum primary illumination map help understand the overall topographic influence, but the temporal information is aggregated. The ITF integrates this information spatially but clarifies the time variation. Over time (peak summer to zero subsolar latitudes), PSR B always has higher ITF values and higher spatially averaged availability of primary illumination (Fig. 6). On average, PSR B will always have higher secondary illumination, so temperatures inside are higher than expected for cold traps. The product of the primary illumination and ITF is roughly proportional to the amount of secondary illumination. Between subsolar latitudes -1.586°and 0°, the total secondary illumination received in PSR B is much larger than PSR A.

ShadowCam maximum radiance image mosaics (Fig. 7, 60m/pixel) derived for the months of February, March, and July in 2023 (ShadowCam nominal mission period) confirm that irradiance received by PSR A is significantly low even when more images are aggregated (maximum statistic) over time. For PSR A, there appears to be little change in radiance magnitude, while the increase is perceptible for PSR B.

6. Conclusion

Cumulative maps of view factors and primary illumination provide simplified guidance for characterizing PSR secondary illumination and cold trap potential spatially and over time. Our analysis clearly shows why Spudis has higher summer maximum temperatures and is not a probable PSR for volatile cold trapping at the scale of our analysis.

Although the analysis indicates that PSR A (Spudis) may not host cold traps with $T < 100K$, the spatial scale of our current analysis is large such that pockets of darkness may exist at finer scales. ShadowCam image mosaics at finer scales will help resolve such unanswered questions.

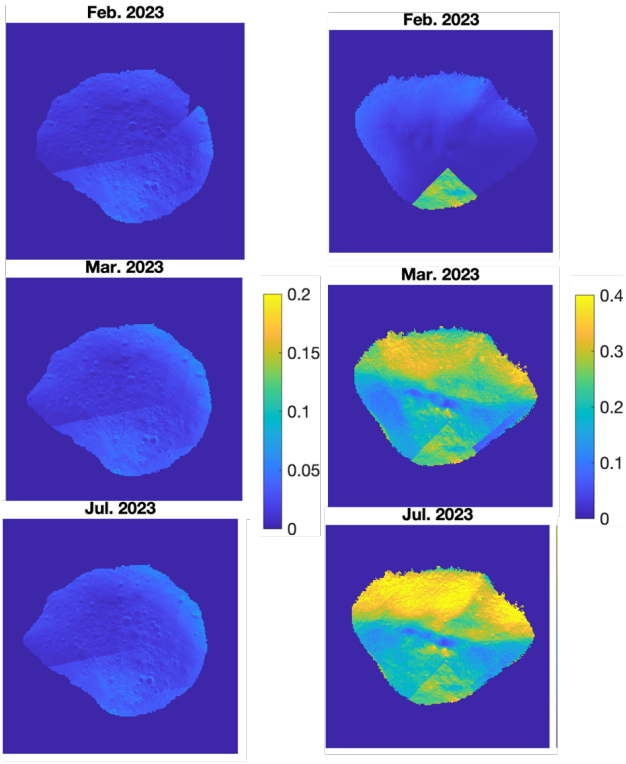

Figure 7. ShadowCam maximum radiance mosaic (60m/pixel) for PSR A and B for the months of February, March and July 2023. Note that PSRs A and B have different ranges for the colorbar

References

Buhl, D., Welch, W. J., Rea, D. G., 1968. Reradiation and thermal emission from illuminated craters on the lunar surface. *Journal of Geophysical Research*, 73(16), 5281–5295.

Carruba, V., Coradini, A., 1999. Lunar cold traps: Effects of double shielding. *Icarus*, 142(2), 402–413.

Cohen, M. F., Wallace, J. R., Hanrahan, P., 1993. *Radiosity and realistic image synthesis*. Morgan Kaufmann.

Hodges Jr, R. R., 1980. Lunar cold traps and their influence on argon-40. *Lunar and Planetary Science Conference Proceedings*, 11, 2463–2477.

Ingersoll, A. P., Svitek, T., Murray, B. C., 1992. Stability of polar frosts in spherical bowl-shaped craters on the Moon, Mercury, and Mars. *Icarus*, 100(1), 40–47.

Kim, E., 2022. The first space exploration mission of korea: Korea pathfinder lunar orbiter (danuri). *Korea Aerospace Society Conference*, 1814–1815.

Lucey, P. G., Hayne, P. O., Costello, E., Green, R., Hibbitts, C., Goldberg, A., Mazarico, E., Li, S., Honniball, C., 2021. The spectral radiance of indirectly illuminated surfaces in regions of permanent shadow on the Moon. *Acta Astronautica*, 180, 25–34.

Mahanti, P., Thompson, T., Robinson, M., Humm, D., Boyd, A., Speyerer, E., Estes, N., Wagner, R., ShadowCam, T., LROC, T., 2021. Secondary illumination in large permanently shadowed regions at the lunar psrs. *European Lunar Science Conference*.

Paige, D. A., Wood, S. E., Vasavada, A. R., 1992. The thermal stability of water ice at the poles of Mercury. *Science*, 258(5082), 643–646.

Robinson, M. S., Brylow, S. M., Caplinger, M. A., Carter, L. M., Clark, M. J., Denevi, B. W., Estes, N. M., Humm, D. C., Mahanti, P., Peckham, D. A. et al., 2023. ShadowCam instrument and investigation overview. *Journal of Astronomy and Space Sciences*, 40(4), 149–171.

Siegler, M. A., Bills, B. G., Paige, D. A., 2011. Effects of orbital evolution on lunar ice stability. *Journal of Geophysical Research: Planets*, 116(E3).

Vasavada, A. R., Paige, D. A., Wood, S. E., 1999. Near-surface temperatures on Mercury and the Moon and the stability of polar ice deposits. *Icarus*, 141(2), 179–193.